Slice-to-Volume Registration and its Potential Application to Interventional MRI-Guided Radio-Frequency Thermal Ablation of Prostate Cancer

Baowei Fei, Jeffrey L. Duerk, *Member, IEEE*, Daniel T. Boll, Jonathan S. Lewin, and David L. Wilson*, *Member, IEEE*

***Abstract*—In this study, we registered live-time interventional magnetic resonance imaging (iMRI) slices with a previously obtained high-resolution MRI volume that in turn can be registered with a variety of functional images, e.g., PET, SPECT, for tumor targeting. We created and evaluated a slice-to-volume (SV) registration algorithm with special features for its potential use in iMRI-guided radio-frequency (RF) thermal ablation of prostate cancer. The algorithm features included a multiresolution approach, two similarity measures, and automatic restarting to avoid local minima. Imaging experiments were performed on volunteers using a conventional 1.5-T MR scanner and a clinical 0.2-T C-arm iMRI system under realistic conditions. Both high-resolution MR volumes and actual iMRI image slices were acquired from the same volunteers. Actual and simulated iMRI images were used to test the dependence of SV registration on image noise, receive coil inhomogeneity, and RF needle artifacts. To quantitatively assess registration, we calculated the mean voxel displacement over a volume of interest between SV registration and volume-to-volume registration, which was previously shown to be quite accurate. More than 800 registration experiments were performed. For transverse image slices covering the prostate, the SV registration algorithm was 100% successful with an error of <2 mm, and the average and standard deviation was only 0.4 mm $\pm$ 0.2 mm. Visualizations such as combined sector display and contour overlay showed excellent registration of the prostate and other organs throughout the pelvis. Error was greater when an image slice was obtained at other orientations and positions, mostly because of inconsistent image content such as that from variable rectal and bladder filling. These preliminary experiments indicate that MR SV registration is sufficiently accurate to aid image-guided therapy.**

***Index Terms*—Image registration, interventional magnetic resonance imaging (iMRI), minimally invasive treatment, mutual information, prostate cancer, thermal ablation.**

I. Introduction

WE USE AN interventional magnetic resonance imaging (iMRI) system to guide minimally invasive treatments, including the radio-frequency (RF) thermal ablation of abdominal cancers [1]–[3]. The iMRI system consists of a 0.2-T clinical C-arm open MRI scanner, an in-room RF-shielded liquid crystal monitor, an MR compatible mouse, a foot pedal, and an RF device. We are currently investigating the extension of these techniques to the treatment of prostate cancer. Since MRI does not reliably show prostate tumors, we intend to incorporate nuclear medicine or MR spectroscopy images with higher sensitivity for detecting and localizing prostate tumors [4], [5]. We will first register the low-resolution functional images with a high-resolution MRI volume [6], [7]. Then, by registering the high-resolution MR volume with live-time iMRI acquisitions, we can, in turn, map the functional data and high-resolution anatomic information to live-time iMRI images for improved tumor targeting. As discussed later, since live-time iMRI is used for device guidance, the accuracy requirements for registering these supplemental images might be less strict than required in some other applications.

We previously described a rigid-body volume-to-volume (VV) registration method for the pelvic and prostate MR images that was accurate when images were acquired under similar conditions [8]. We used bony landmarks and three-dimensional (3-D) centroids of segmented prostates to evaluate VV registration. For volume pairs acquired over a short time span from a supine subject with legs flat on the table, registration accuracy of both the prostate centroid (typically <1 mm) and bony landmarks (average 1.6 mm) was on the order of a voxel ($\approx$1.4 mm). The centroid error was slightly smaller because the prostate was at the volume center and rotation errors had less effect on it. The localization error in finding 3-D points from bony landmarks is probably greater than that

Manuscript received August 20, 2002; revised November 10, 2002. The algorithm developed in this research was supported by the National Institutes of Health (NIH) under Grant R01-CA84433-01 to D. L. Wilson and by the Department of Defense under Grant DAMD17-02-1-0230 to B. W. Fei. Imaging techniques were developed under the support of the NIH under Grant R33-CA88144-01 to J. L. Duerk. The Associate Editor responsible for coordinating the review of this paper and recommending its publication was W. Niessen. *Asterisk indicates corresponding author*.

B. W. Fei is with the Department of Biomedical Engineering, Case Western Reserve University, Cleveland, OH 44106 USA.

J. L. Duerk is with the Department of Radiology, University Hospitals of Cleveland and Case Western Reserve University, Cleveland, OH 44106 USA, and also with the Department of Biomedical Engineering, Case Western Reserve University, Cleveland, OH 44106 USA.

D. T. Boll is with the Department of Radiology, University Hospitals of Cleveland and Case Western Reserve University, Cleveland, OH 44106 USA.

J. S. Lewin is with the Department of Radiology and the Departments of Oncology and Neurological Surgery, University Hospitals of Cleveland and Case Western Reserve University, Cleveland, OH 44106 USA, and also with the Department of Biomedical Engineering, Case Western Reserve University, Cleveland, OH 44106 USA.

*D. L. Wilson is with the Department of Biomedical Engineering, Case Western Reserve University, 10900 Euclid Ave., Cleveland, OH 44106 USA, and also with the Department of Radiology, University Hospitals of Cleveland and Case Western Reserve University, Cleveland, OH 44106 USA (e-mail: dlw@po.cwru.edu).

Digital Object Identifier 10.1109/TMI.2003.809078

of finding centroids of relatively large prostate volumes where segmentation errors average out. We obtained somewhat larger prostate registration errors of about 3.0 mm when volume pairs were obtained under very different conditions that would be avoided in patient studies, e.g., legs flat and legs raised.

In this study, we are investigating methods to register live-time iMRI image slices with a previously obtained high-resolution MRI volume. We call this slice-to-volume (SV) registration. Because of our success with VV prostate registration, we can determine SV accuracy by comparing results to VV registration for volume pairs having low VV registration error.

The application of SV registration to iMRI-guided treatment of prostate cancer raises several challenges. First, a single slice, or a few slices, provides much less information than an entire volume for voxel-based matching. Second, iMRI images often have lower signal-to-noise ratio (SNR) than diagnostic MR images because of the emphasis on fast imaging and because of the typically lower field strength of open iMRI magnets. Third, the normal prostate is a small organ; when healthy, it measures only $\approx$3.8 cm in its widest dimension [9]. The small prostate is located below the much larger bladder that can change its shape and size during imaging. Fourth, the nonhomogenous receive coil response can change from one imaging session to the next. Finally, times for registration and algorithm robustness are of particular concern for this application to treatment.

Previously reported methods for SV registration were mainly applied to the brain for applications of functional MRI [10], postmortem pathology studies [11], and anatomical modeling [12]. There are no reports of SV registration for abdominal organs or iMRI guidance. Voxel-based methods, particularly those based upon mutual information (MI), are robust, require no segmentation that can be prone to error, are suitable for multimodality registration, and are highly accurate for many applications [3], [8], [10], [13]–[15]. However, the MI method has the problem of interpolation artifacts, which can be especially serious in the case of downsampling in a multiresolution approach [16]. Other similarity measures such as the correlation coefficient (CC) can reduce the presence of local minima [17].

In this paper, we first describe a voxel-based registration algorithm with special features for this important new application. Later, we describe the details of imaging experiments on a conventional MR scanner and a clinical iMRI system. Actual and simulated iMRI images are used to test the registration algorithm. Results of SV and VV registration are compared. In this study, we have performed more than 800 registration experiments.

II. Registration Algorithm

A. Similarity Measurements

We used two similarity measures—mutual information and correlation coefficient—in our registration. Suppose one image R is the *reference*, and the other F is *floating*. Their mutual information $\mathrm{MI}(R,F)$ is given as follows [18]:

$$\mathrm{MI}(R,F)=\sum_{r,f} p_{\mathrm{RF}}(r,f)\log\frac{p_{\mathrm{RF}}(r,f)}{p_R(r)\cdot p_F(f)}.$$

The joint probability $p_{\mathrm{RF}}(r,f)$ and the marginal probabilities $p_{\mathrm{R}}(r)$ of the reference image and $p_{\mathrm{F}}(f)$ of the floating image can be estimated from the normalized joint intensity histogram. The correlation coefficient $\mathrm{CC}(R,F)$ is given as follows [19]:

$$\mathrm{CC}(R,F)=\frac{\sum\left(R(r)-\overline{R}(r)\right)\left(F(f)-\overline{F}(f)\right)}{\sqrt{\sum\left(R(r)-\overline{R}(r)\right)^2\sum\left(F(f)-\overline{F}(f)\right)^2}}.$$

Here $\overline{R}(r)$, $\overline{F}(f)$ denote the average intensities of the reference and floating images and the summation includes all voxels within the overlap of both images.

We compared the two similarity measures at different resolutions in order to determine their suitability for SV registration. At *1/4 resolution*, we resampled images so as to give 1/4 number of the voxels along each linear dimension. At *full resolution*, we used the full number of voxels. In Figs. 1 and 2, we plot the two similarity measures as a function of two translation parameters. After two typical high-resolution MR volumes were registered [8], values were plotted with the origin as the optimal transformation. We calculated CC and MI values while moving the simulated iMRI image relative to the high-resolution MR image along coronal (anterior–posterior) and sagittal (left–right) axes. The simulated iMRI image was obtained as described in Section III.

Features of MI and CC demonstrate their suitability at high and low resolutions, respectively. At 1/4 resolution, CC surfaces are much smoother than MI, which is noisy and contains many local maxima as shown in Fig. 1(a) and (c). In fact, there is a false global maximum at $+25$ voxels. At full resolution, Fig. 2(a) and (c) shows that MI has a much sharper peak than CC, but once again there is high-frequency noise in the MI curves, far from the optimum, that gives rise to local maxima that must be avoided. From these figures, we infer that CC is better at low resolution and MI is better at full resolution, when one is close to the optimum value. As described next, our registration algorithm makes use of these features.

B. Registration Algorithm with Special Features

The algorithm includes special features to improve robustness for registration of MR prostate images. Suppose the iMRI image slice is the *reference slice*, the matching slice extracted from the high-resolution MRI volume is the *reformatted slice*, and the final reformatted slice is the *registered slice*. We use a multiresolution approach and perform registration from low to high resolution. We use CC at the two lower resolutions because it gives fewer local maxima and because it can be calculated faster than MI. We use MI at full resolution because of its peaked surface. To avoid local maxima, we include a restarting feature where registration is restarted with randomly perturbed parameters obtained from a uniform distribution about the initial transformation values at the current resolution being used. The algorithm restarts until the absolute CC is above a threshold of 0.5 as determined later or the maximum number of restarts is reached. Absolute CC is used rather than MI because it has a well-defined range between 0 and 1 and because it provides an independent check of the MI result at the highest resolution.

We record all important results following an optimization cycle including the CC and/or MI values and the transforma-

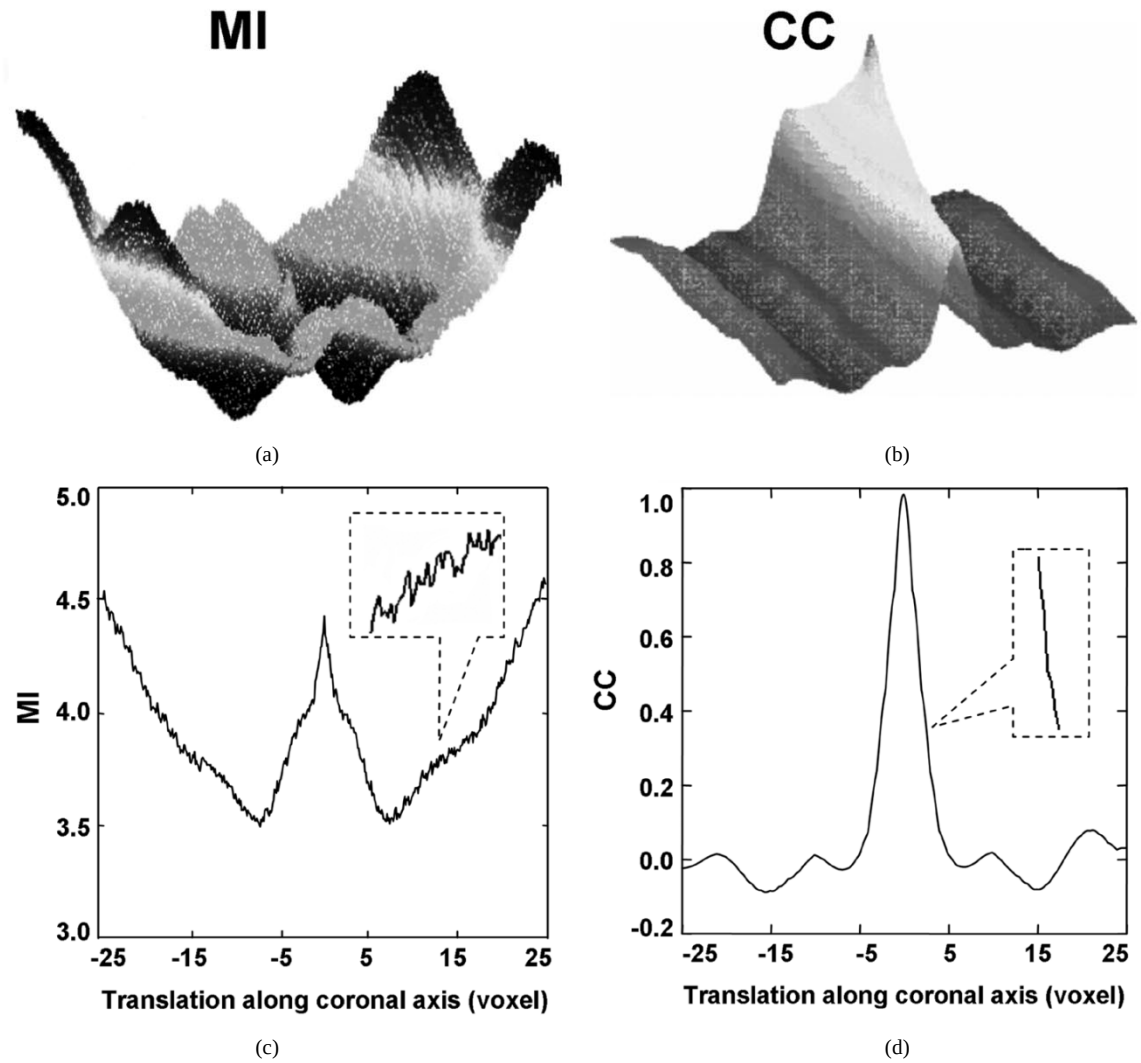

Fig. 1. Similarity functions are plotted as a function of translations at the lowest resolution in the multiresolution registration process. Two high-resolution MRI volumes were registered. From the optimal parameters, we computed the similarity of the simulated iMRI and MRI images as a function of translations along the coronal (anterior–posterior) and sagittal (left–right) axes. MI is plotted in (a) and (c); CC is plotted in (b) and (d). Graphs (a) and (b) are 3-D plots for translations along the coronal and sagittal axis. Graphs (c) and (d) are 2-D plots for translations about the coronal axis. The small insets in (c) and (d) are magnified curves showing noise having local maxima in (c). A false global maximum for MI occurred at $+25$ voxels. Images are from volunteer S2, and they are downsampled by 1/4 along each linear dimension, giving a distance between voxel centers of ≈ 5.5 mm.

tion parameters. At the end of processing at a lower resolution, we always select the transformation parameters having the maximum CC value. We then scale the translation parameters appropriately and assign the new parameters to be initial values at the next higher resolution. At the highest resolution, MI instead of CC is the similarity measure, and we select the final transformation parameters to be those having the maximum MI value.

C. Additional Details

Additional algorithm details are now described. For registration, we use rigid-body transformation (three translations and three rotations) and trilinear interpolation. For optimization, we use the downhill simplex method of Nelder and Mead [20] or the Powell method [21]. Optimization of similarity ends either when the maximum number of calculations is reached (typically 500) or the fractional change in the similarity function is smaller than a tolerance (typically 0.001). The input MRI volume is a 3-D MR acquisition giving $256 \times 256 \times 128$ nearly isotropic voxels over a field of view covering the whole pelvis. We create isotropic voxels of about 1.4 mm on a side using 3-D linear interpolation. We use IDL (Interactive Data Language, Research Systems Inc., Boulder, CO) as the programming language.

Typical parameter values are now described. We use an initial guess assuming an identity transformation, i.e., all initial translation and rotation parameters are zero, because the patient is normally oriented approximately the same way from one scan to the next. We set the maximum numbers of restarts at 10, 5, and 3, from low to high resolution, respectively.

III. Experimental Methods

A. Image Acquisition

High-resolution MRI volumes were acquired using a 1.5-T Siemens MRI system (Magnetom Symphony, Siemens Medical Systems, Erlangen, Germany). An eight-element phased array body coil was used to ensure coverage of the prostate with a

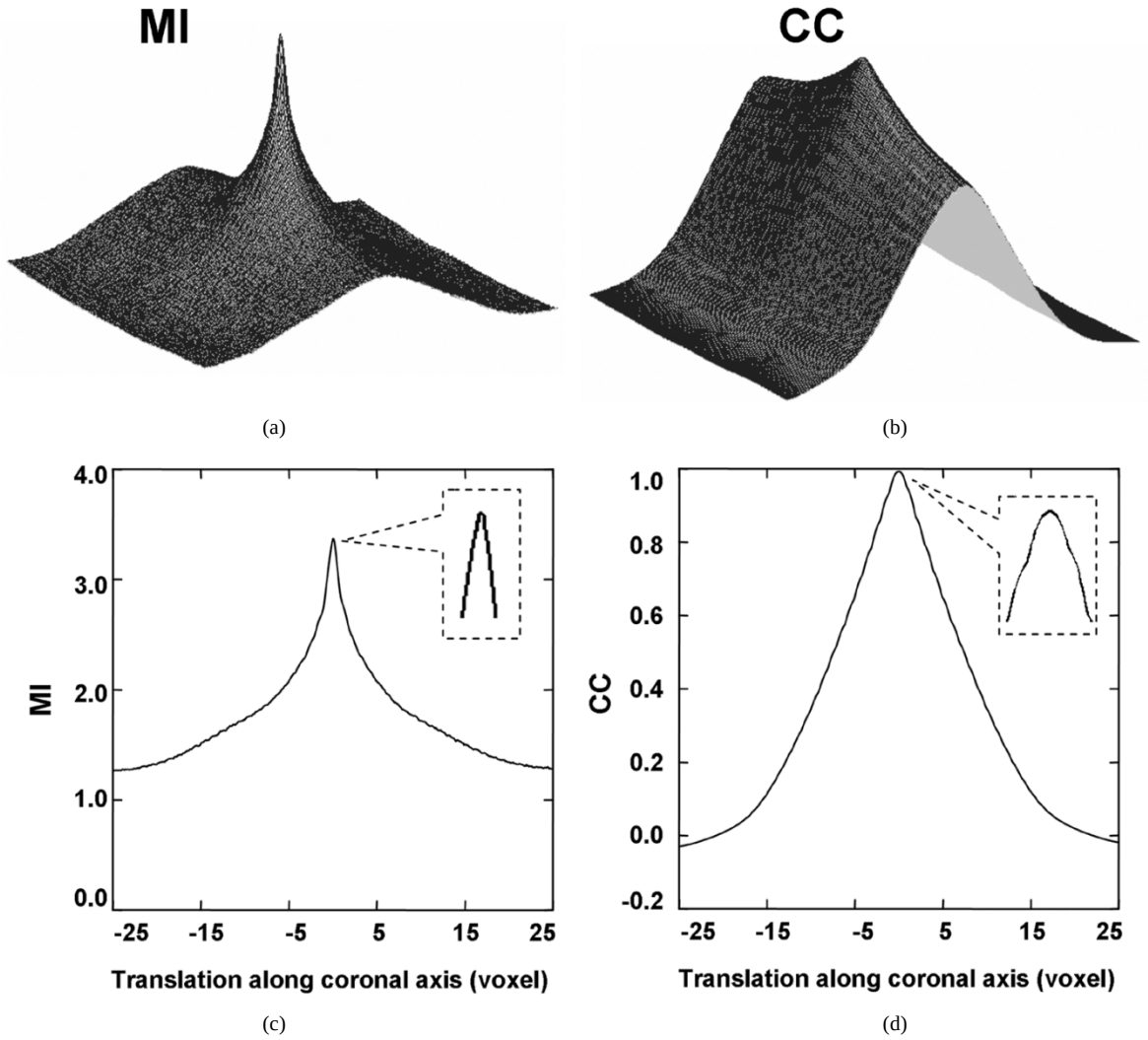

Fig. 2. Similarity functions are plotted as a function of translations at full resolution. Many details are given in the legend of Fig. 1. Again, MI is plotted in (a) and (c); CC is plotted in (b) and (d). MI in (a) and (c) has a much sharper peak than CC in (b) and (d). The voxel is isotropic with 1.4 mm on a side. Image data are the same used in Fig. 1.

uniform sensitivity. Typically, two anterior and two posterior elements were enabled for signal acquisition. We used two different MR sequences. First, we used a 3-D RF spoiled gradient echo steady-state pulse sequence (FLASH) with TR/TE/flip parameters of 12/5.0/60, which give $256 \times 256 \times 128$ voxels over a $330 \times 330 \times 256$-mm field of view (FOV) to yield $1.3 \times 1.3 \times 2.0$-mm voxels oriented to give the highest resolution for transverse slices. The acquisition time is 5 min and 38 s. This sequence is good for pelvic imaging, but is not ideal for the prostate. It was used to acquire volumes for volunteer S1. Second, we used a 3-D rapid gradient echo sequence (PSIF) designed to acquire the spin-echo component of the steady-state response, rather than the free induction decay. The spin echo component forms immediately prior to the RF pulse; it is shifted toward the prior RF pulse through appropriate gradient waveform design. The sequence with 9.4/5.0/60 (TR/TE/flip) yields $160 \times 256 \times 128$ voxels over a $219 \times 350 \times 192$-mm rectangular FOV and $1.4 \times 1.4 \times 1.5$-mm voxels oriented to give the highest resolution for transverse slices. There is over sampling at 31% in the slice direction to reduce aliasing artifacts. The acquisition time is 4 min and 15 s. This sequence gave excellent image contrast for the prostate and its surroundings. It was used to acquire volumes for volunteers S2–S4.

We also acquired iMRI images from the same volunteers using a clinical 0.2-T C-arm open MR scanner (Siemens Open Symphony, Erlangen, Germany) modified for interventional MRI procedures and in this paper referred to as the iMRI system. We used a 3-D PSIF with 25/13/60 (TR/TE/FA) for image volume acquisitions and two-dimensional (2-D) PSIF with 15.2/7.4/45 (TR/TE/FA) for image slice acquisitions. The iMRI volumes were $256 \times 256 \times 100$ with voxel size of $1.3 \times 1.3 \times 1.4$ mm. The iMRI slices were 128×128 with in-plane pixel size of 2.8×2.8 mm and with effective slice thickness of 5 mm. We acquired iMRI images from volunteers S1–S3.

B. Simulation of iMRI Image Slices

In experiments, we used high-resolution MRI volumes to simulate iMRI image slices, which are thicker, noisier, and degraded by receive coil inhomogeneity. Clinically, we typically use an iMRI slice thickness of 4.0–6.0 mm. We used trilinear interpolation to create isotropic high-resolution MRI volumes

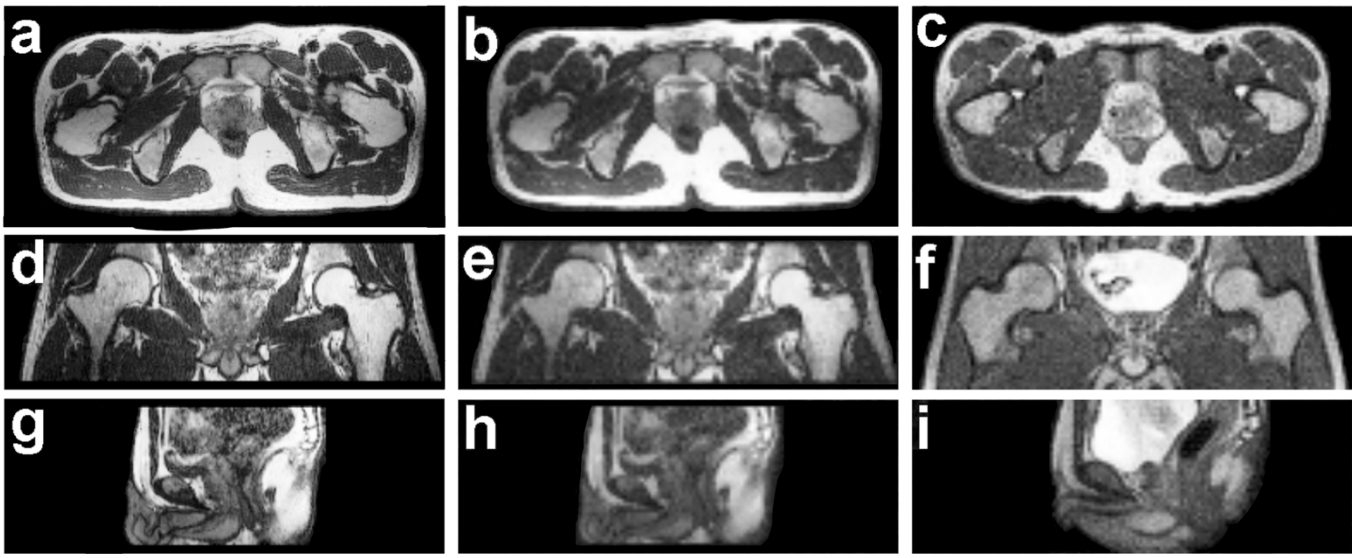

Fig. 3. High-resolution MR images, simulated and actual iMRI image slices. Images on the left column, (a), (d), and (g), are the original high-resolution MR images from the 1.5-T scanner in the transverse, coronal, and sagittal planes, respectively. Images in the middle column are the corresponding, simulated thick iMRI images with noise added to give $\mathrm{SNR} = 15$ and with sensitivity fall off from a belt coil. Images on the right panel are actual iMRI slices (0.2-T scanner) from similar spatial locations. The actual iMRI slices seem blurred because of nearly doubled pixel size. Images are from volunteer S2.

with voxel size of $1.4 \times 1.4 \times 1.4$ mm. From the isotropic high-resolution MRI volume, we averaged three 1.4-mm adjacent thin slices to create a 4.2-mm-thick slice. MR noise in a magnitude is described by the Rician distribution [22]. At SNR values of greater than approximately five, the noise can be approximated as being Gaussian white noise [23]. We measured typical signal and noise values on our iMRI system using a homogenous phantom, and volunteer images in the region of the prostate with methods described elsewhere [24], [25]. In all cases, image SNR was greater than 10 in all tissues including the prostate. With this justification, we added Gaussian noise to the simulated iMRI image slices either to match the measured SNR or to give much greater noise to further stress registration. We report noise experiments using the SNR of the simulated image slices. Fig. 3 shows high-resolution MR images as well as simulated and actual iMRI image slices.

We simulated receive coil inhomogeneity from a belt coil used in our clinical iMRI acquisitions. The coil is modeled as a solenoid with parameters shown in Fig. 4. Coil parameters are a, the radius of the coil; $2\,g$, the length of the coil; I, the current; μ_0, the permeability of free space; n, the turns; and the z axis, the axis along the center line of the coil. The magnetic field in the xy plane can be approximated as [26]

$$(B_1)_{xy} = \frac{\mu_0 n}{2} \frac{I}{[a^2 + g^2]^{1/2}}. \tag{1}$$

The z component of the field is given by [27]

$$(B_1)_z = \frac{\mu_0 n I}{2g} (\cos\alpha_1 + \cos\alpha_2) \tag{2}$$

where the definition of the angles α_1 and α_2 are given in Fig. 4. The magnetic field is highest at the coil center and falls off along the axial direction. According to the Biot–Savart law [28], this model also accounts for the spatial sensitivity of the coil to MR signal sources. Fig. 5 shows a coronal image with simulated inhomogeneity along the axis (head–foot) direction.

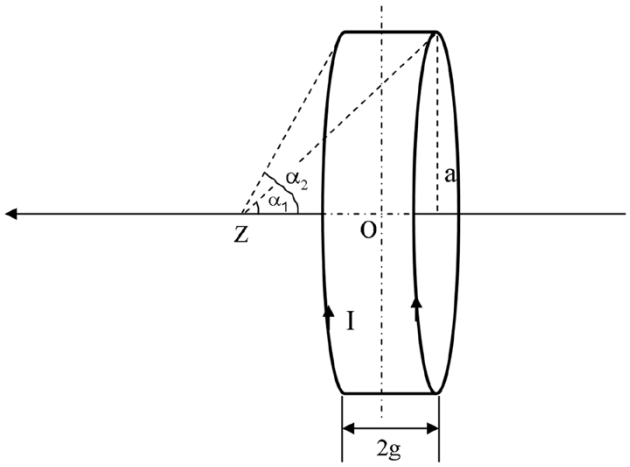

Fig. 4. Geometry of solenoidal receive coil. Model parameters are defined in the figure. The axial line is along the cranial–caudal direction of the patient.

Because a needle will often be present during an iMRI intervention, we tested the effect of simulated needles on registration. We used artifact sizes from a previous report on the effects of pulse sequence design and magnetic field orientation on needle artifacts in MR-guided biopsy and aspiration [29]. Fig. 6 shows sagittal images with and without a simulated needle artifact. The simulated artifacts in Fig. 6(b) appeared as straight noisy bars 2 mm in width.

C. Imaging Experiments

1) Imaging Experiments for High-Resolution MR Volumes: When acquiring high-resolution MR volumes, volunteers laid supine in a manner similar to the *diagnostic position* in routine MR scanning. Between volume acquisitions, volunteers got up from the MR table, stretched, and walked

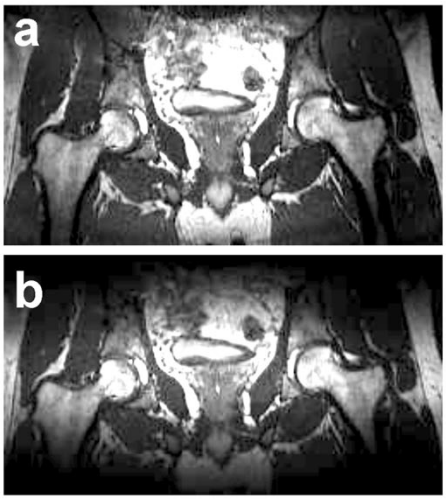

Fig. 5. Simulated signal changes due to receive coil inhomogeneity. The original image (a) is acquired using a phased array coil on a conventional 1.5-T MRI system. Using a belt coil model with a diameter of 350 mm and a width of 50 mm, the simulated iMRI image is shown in (b). The image intensity is highest at the center and decreases along the axial direction.

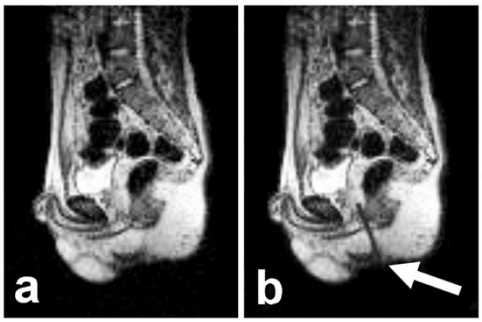

Fig. 6. Synthetic image with simulated needle artifact. Image (a) is the sagittal slice acquired from the 0.2 T iMRI system without a needle artifact. Image (b) is obtained from image (a) with a simulated needle artifact (white arrow) for an RF needle probe inserted into the prostate. Images are from volunteer S3.

around to ensure that they would assume a different position when they laid back on the table. Before the last of three volume acquisitions, the volunteer voided to create an *empty bladder*. The coil array was centered on the prostate. All images of the same volunteer were acquired with the same MRI acquisition parameters. In total, there are 12 volumes, three for each of volunteers S1–S4.

2) Imaging Experiments on iMRI System: We acquired iMRI images under the conditions simulating the treatment application. The volunteer was supine, and his legs were supported at 30°–60° relative to the horizon and separated in a "V" with an angle of 60°–90° between two legs. This is similar to the lithotomy position used in prostate therapies, and it should provide access for needle insertion in brachytherapy or RF thermal ablation. We call this the *treatment position*. Before experiments, the volunteer voided their bladder. For each volunteer, all images were obtained within a 2-h session. Between image acquisitions, volunteers moved to ensure a different position. For each of the volunteers S1–S3, we acquired three volumes and 50 iMRI image slices covering the prostate. They included 30 transverse, ten coronal, and ten sagittal image slices. We call these images "*actual*" iMRI images to differentiate them from previous experiments using "*simulated*" iMRI slices.

D. Registration Experiments

1) Registration Experiments Using Simulated iMRI Images: We used 12 pairs of high-resolution MR volumes to perform registration experiments. For each volume pair, we extracted data from one volume to simulate thick iMRI image slices; and then we registered the simulated image slices to the other volume. We desire an iMRI slice image acquisition method that gives robust, accurate registrations and is relatively insensitive to acquisition parameters. Hence, we performed experiments to determine the dependence on slice orientation (transverse, sagittal, and coronal), on slice position relative to the prostate (above, centered, and below), on image noise from fast imaging techniques, and on the inhomogeneous sensitivity response from a belt coil.

2) Registration Experiments Using Actual iMRI Image Slices: We also performed two types of SV registration experiments using the actual iMRI images. First, we registered actual iMRI image slices with high-resolution (1.5-T system) MR volumes and visually evaluated results. For each volunteer S1–S3, there were three high-resolution MR volumes and 50 iMRI image slices giving 150 SV registration experiments, and a total of 450 experiments. Second, we registered thick slices simulated from the volume of image data obtained on the iMRI scanner with the corresponding high-resolution (1.5-T scanner) MR volume. In this case, we compared results to VV registration obtained by registering the volume from the iMRI system with the high-resolution volume (1.5-T scanner). We investigated the effect of iMRI slice thickness by averaging 1–10 contiguous image slices to create a thick slice and registering it to the high-resolution volume. The original actual iMRI volumes have a slice thickness of 1.4 mm and in-slice dimensions of 1.3×1.3 mm. We used trilinear interpolation to create isotropic actual iMRI volumes with voxel size of $1.3 \times 1.3 \times 1.3$ mm. Thus, thick slices simulated from actual iMRI volumes are 1.3 to 13 mm.

E. Registration Evaluation

1) Visual Inspection: We evaluated registration experiments by visual inspection. We used *RegViz*, a program created in IDL in our laboratory with multiple visualization and analysis methods. First, we manually segmented prostate boundaries in image slices and copied them to corresponding slices. This enabled visual determination of the overlap of prostate boundaries over the entire volume. Second, color overlay displays were used to evaluate overlap of structures. One image was rendered in gray and the other in the "hot-iron" color scheme available in IDL. To visualize potential differences, it was quite useful to interactively change the contribution of each image using the transparency scale. Third, we used a sector display, which divided the reference and registered images into rectangular sectors and created an output image by alternating sectors from the two input images. Even subtle shifts of edges would be clearly seen.

2) Volume-to-Volume Registration Standard: Our standard evaluation method was to compare SV and VV registration.

The VV registration accuracy was previously evaluated [8]. For volume pairs acquired over a short time span from a supine subject with legs flat on the table, prostates were well aligned and prostate centroid displacements were typically <1 mm. The registration accuracy as determined from displacements of pelvic bony landmarks was 1.6 mm $\pm$ 0.2 mm. This error might be overestimated because it includes the uncertainty of locating the bony landmarks. From our success with VV prostate registration, we decided that we could obtain SV accuracy by comparing to VV registration for those volume pairs having low VV registration error.

To compare SV and VV registration results, we defined a rectangular volume of interest (VOI) just covering the prostate over which to calculate registration error. To voxels within the VOI, we applied the transformations obtained by the VV and by SV registrations. We then calculated the 3-D displacements between the transformed voxels. The mean voxel distance over the VOI was used as our metric of SV registration error. For evaluation of algorithm robustness, we defined the SV registration as being *successful* when the mean 3-D displacement was less than 2.0 mm.

IV. Results

A. Experiments with Simulated iMRI Images from the 1.5-T System

As described in Section III, we obtained relatively low-noise high-resolution MR images and simulated SV registration results. These datasets allowed us to test effects of noise and receive coil inhomogeneity in a controlled fashion. And, because we had substantial previous experience showing the accuracy of VV registration under comparable conditions, we could easily determine SV error by comparing results to VV registration.

In Fig. 7, the sector display shows a simulated image slice registered with a high-resolution image volume. The simulated image slice was obtained at a transverse orientation near the center of the prostate. The sector display shows close alignment at this position. Other transverse images were also well aligned, indicating that the registration was successful in three dimensions.

We determined SV registration results for slices near the prostate in the three standard orthogonal orientations. Compared with VV, mean and standard deviation registration errors across 12 volume pairs and 60 SV registration experiments were 0.4 mm $\pm$ 0.2 mm, 0.5 mm $\pm$ 0.2 mm, and 2.6 mm $\pm$ 1.6 mm for transverse, coronal, and sagittal slices covering the prostate, respectively. Transverse slices worked best because they contain many relatively rigid anatomical structures (see Fig. 3). We further found that transverse slices centered on the prostate produced better results than those above or below the prostate. Image slices above included the deformable bladder that could give an inconsistent structure from one volume to the next. Image slices below the prostate mainly contained muscle and fatty regions from the hips that could deform, again giving inconsistent image data. Coronal slices worked next best. Sagittal slices gave the largest error because they contained a large portion of the deformable bladder and rectum.

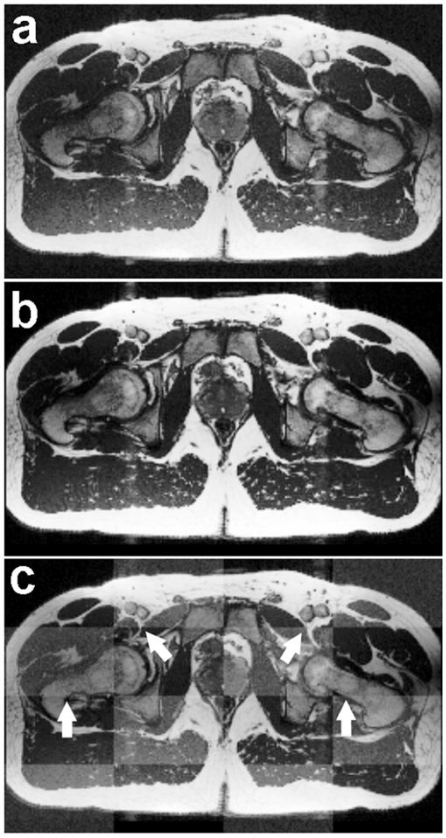

Fig. 7. Sector display showing quality of SV registration. Transverse slices are shown for (a) simulated iMRI and (b) high-resolution MRI images. In the sector display (c), a checker board pattern is created where image sections from (a) and (b) are alternated. Square sections from (a) are made brighter in order to show the boundaries. As indicated by the arrows, the boundaries of bones and other structures are continuous across the sections indicating excellent registration. The prostate registered very well. Images are acquired from volunteer S4.

Simulation experiments showed SV registration to be very insensitive to noise. We performed over 150 registration experiments with noise added to give SNRs ranging from 20 to 5. Using the slice configurations recommended above (transverse slices near the prostate center), we obtained 100% successful registrations (an error <2.0 mm) for SNRs ≥ 10, a value much worse than the clinical SNR value of ≈ 25 on our iMRI system.

Receive coil inhomogeneity also had little effect on registration. Registration again was 100% successful for all volume pairs under all receive coil configurations, even when the coil for the slice acquisition was displaced up to 200 mm toward the head from the prostate center, the position of the coil for the volume acquisition.

B. Experiments with Actual iMRI Images

Fig. 8 shows results for an SV registration of actual iMRI image slices with a high-resolution MR volume. The contours overlap and overlay images show that the prostate matches very well. Other visual inspection techniques also demonstrate excellent registration. Note that a single iMRI image was used to produce this registration result.

Fig. 9 shows SV registration error as a function of slice thickness. As described previously, we first registered each volume from the iMRI scanner with the corresponding high-resolution

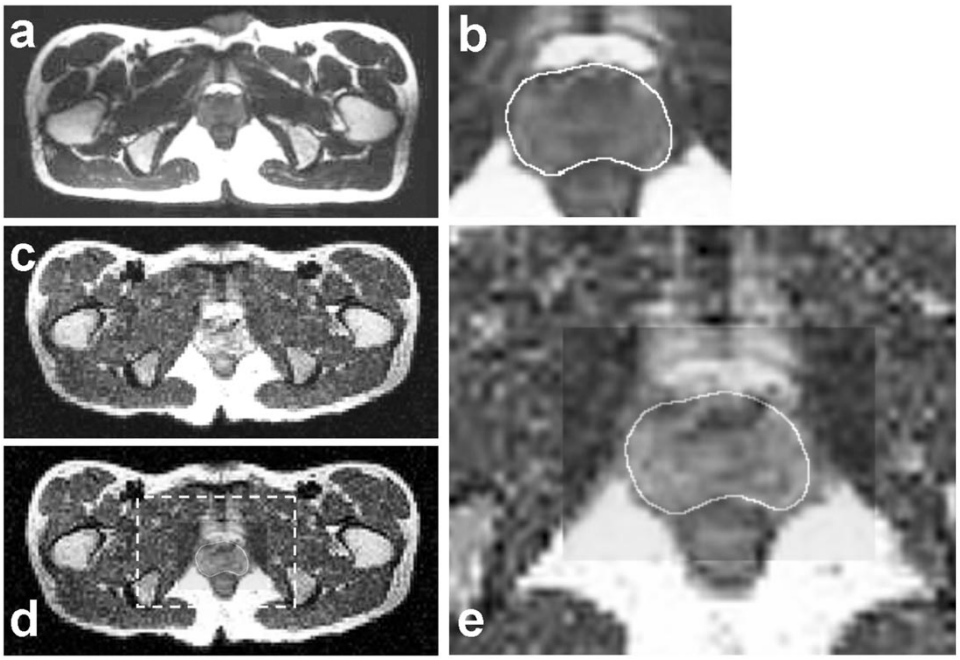

Fig. 8. Images after SV registration of actual iMRI slices from a 0.2-T open MR system. Image (a) is a transverse slice from a high-resolution MR volume (1.5-T scanner). The prostate is segmented and magnified in image (b). Image (c) is the actual iMRI slice (0.2-T scanner). Images (c) and (b) are displayed together in an overlay in image (d), and the white rectangular region is magnified in image (e). The segmented prostate boundary from the high-resolution MR image is copied to the actual iMRI image where it closely matches the prostate in the actual iMRI image slice indicating excellent registration.

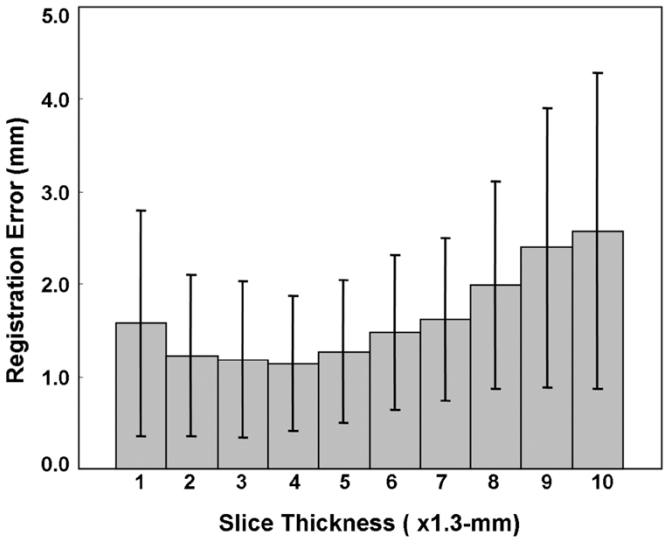

Fig. 9. SV registration using images with different slice thickness. The error metric is the average voxel displacement between the SV and VV registrations. Plotted are mean errors as well as standard deviation from a rectangular VOI surrounding the prostate. One typical datasets of high-resolution MRI volume and actual iMRI slices of volunteer S1 are used for the registration experiments. For each thickness, ten registration experiments were conducted using ten different simulated iMRI transverse slices that intersected the prostate with different distances. Thick iMRI slices were obtained by averaging 1–10 iMRI image slices.

MRI volume (1.5-T scanner) using rigid-body voxel-based registration [8] and used the result as the gold standard for calculating the SV error. Each thick slice image was obtained by averaging several contiguous slices from the actual iMRI volume. As the slice thickness increases from 1×1.3 mm to 4×1.3 mm, the registration error decreases, possibly because of improved SNR and/or because of the inclusion of more features. Error increases with thicker slices, probably because of the inconsistency of image features between the thick slice and more finely sampled volume.

In Fig. 10, we evaluated SV registration for thick slices at different orientations. The evaluation method was the same as that used in Fig. 9, and the slices were 5 mm thick and intersected the volume near the prostate center. Results were consistent with those from the previous simulation experiments. Transverse slices worked best with an average VOI displacement of only 1.1 mm $\pm$ 0.7 mm and a success rate of 100%. The coronal images gave a reasonable average error, but the success rate dropped to 86%. The sagittal orientation gave the worst result.

Needle artifacts had little effect on the SV registration. In each of 30 the experiments, we registered a high-resolution volume with an actual iMRI image slice containing or not containing a simulated needle artifact. Visual inspection, the correlation coefficient, and mutual information values of registered images showed little effect of the needle artifact. The success rate was 100% in both cases.

C. Algorithmic Robustness and Implementation

The registration algorithm was quite robust for transverse slices covering the prostate. Using simulated iMRI slices from high-resolution MRI volume pairs of four volunteers, the algorithm never failed for any transverse slice covering the prostate. In addition, the final registration result was insensitive to initial guesses within a very large range, $[-60, +60]$ mm for translations and $[-20, +20]$ degrees for rotations. With the restarting algorithm, we even successfully registered slices as much as 80 mm from the optimum. This working range should be quite

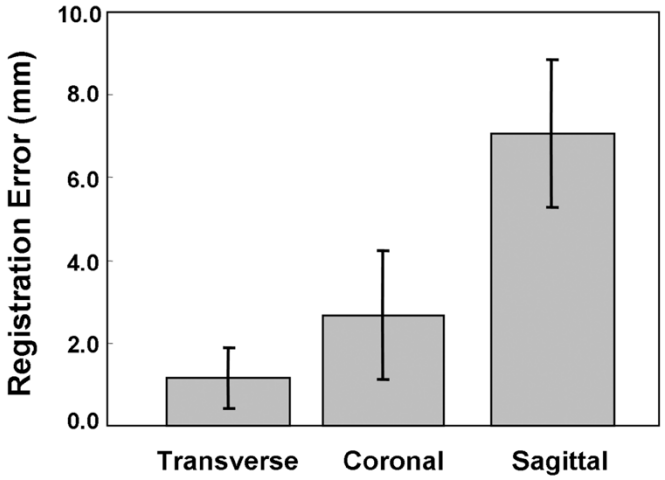

(a)

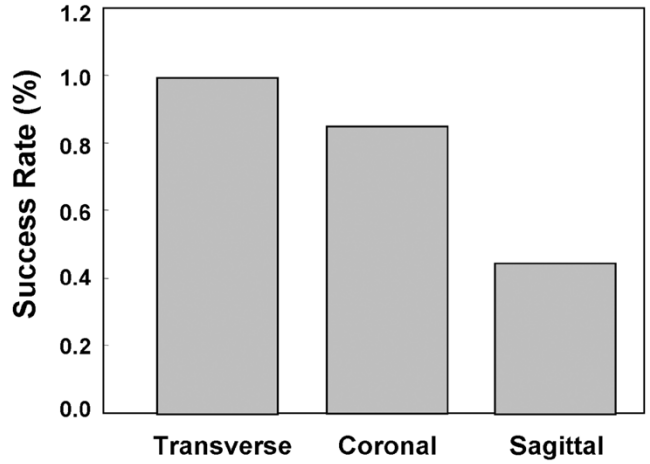

(b)

Fig. 10. SV registration error and robustness for iMRI images in the three standard orientations. In (a), registration error relative to VV registration is plotted as a function of image slice orientation. In (b), success rate is also plotted as a function of orientation where registration is successful when the error is $<$2.0 mm. For volunteer S2, one high-resolution volume and one volume from the iMRI scanner were used in these experiments. Data were extracted from the iMRI volume to simulate iMRI slices with a thickness of about 5 mm. Fifteen transverse, coronal, and sagittal slices from the prostate center were used for SV registration, respectively.

sufficient for clinical applications where we can ensure good starting values. Using the pelvic bones as markers and device localization methods [29], we should be able to position the prostate within about $\pm$20 mm in the imaging field. In addition, the patient normally lies supine in the MR bed with very little rotation ($< \pm 5^{\circ}$).

Using CC and MI at different resolutions was an important feature that increased robustness. MI registrations at low resolution sometimes gave false maxima [Fig. 1(a) and (c)], and only 60% success was achieved when MI was used at all resolutions. The interpolation artifacts at low resolutions often caused failures and required more restarts [16]. CC performed well and gave fewer local maxima at the lower resolutions [Fig. 1(b) and (d)], but MI was more accurate than CC at the highest resolution due to the sharper peak of the MI surface [Fig. 2(a) and (c)] [8]. Our registration algorithm thus combined advantages from the two similarity measures.

The multiresolution approach improved algorithmic robustness and speed. When we used only MI at full resolution, registration was 70% successful compared to the 100% of the full algorithm. This failure of MI was also reported by others [13], [17]. The multiresolution approach enabled the program to quickly approach the final value because of the reduced number of calculations at low resolutions. For a typical image pair, iterations at 1/4 resolution were approximately 4 and 25 times faster than at 1/2 and full resolution, respectively.

Restarting was important for image pairs with large translations and/or rotations from the optimum. In our experience with over 800 SV registration experiments, restarting occurred in about 5% of them. For an example pair with an 80-mm displacement, the number of restarts was 3, 1, and 0 at 1/4, 1/2, and full resolutions, respectively. Without restarting, we found that registrations sometimes failed in cases of volumes with a large mismatch of 54 mm and high noise. The algorithm was insensitive to the CC threshold for restarting. When we decreased the threshold from 0.8 to 0.5 with an interval of 0.05, we found little change in the number of restarts and no change in final registrations. We set the threshold at 0.5 to avoid only the most obvious local maxima.

We now describe some aspects of the implementation. The time for an SV registration was typically about 15 s on a Pentium IV 1.8-GHz CPU with 1 GB of memory. The algorithm was written in IDL and could probably be made much faster in a lower level language such as C. A call to the Simplex optimization typically resulted in 50 to 105 similarity evaluations before the tolerance value (0.001) was reached. The simplex optimization method worked about 1.5–2.0 times faster than the Powell method in our implementation. We used the Simplex method for our experiments in this study.

V. Discussion and Conclusion

Despite complications such as image noise, receive coil inhomogeneity, a limited number of voxels, and needle artifacts, SV voxel-based registration can be quite robust and accurate. For transverse slices covering the prostate, registration results agreed very favorably with VV results. Below, we further discuss the algorithm and its practicality.

A. Mutual Information at Low Resolution

There are probably several reasons why mutual information does not work well at low resolution. First, the similarity curve is noisy with periodic oscillations from the so-called interpolation artifact [8], [16] that is accentuated at reduced resolutions [30]. As a result, there are many local maxima in Fig. 1(a) and (c) that can trap the optimization; and a similar result was reported for brain registration [13]. In additional experiments, we decreased the number of bins for both images to 256, 128, 64, and 32 and plotted mutual information values as a function of translation. With a larger number of bins, we got no discernable effect of bin size. When the number of bins was reduced to 32, the MI surface was degraded. Others showed that Gaussian blurring of images before registration did not improve performance at low resolutions and that there was little difference between standard and normalized mutual information [40]. Second, when images are

of low resolution and there is only a small region of overlap, the mutual information function can even contain incorrect global maxima [30] as found in Fig. 1(a). This false result was obtained at very large displacements where the SV overlap was reduced. This occurs because MI is not only a function of how well the images match in the overlap, but also by how much information is provided by the two images in the overlap [31], [32], [35]. As shown above, using both mutual information and correlation coefficient, at different resolutions, was an important feature that increased robustness.

B. Accuracy Consideration

Essentially, we found that SV is of similar accuracy to VV registration, with an average voxel displacement difference of only 0.4 mm in the prostate for the simulated images and about 1 mm for actual iMRI image data. Hence, the accuracy of the best SV method is essentially that previously reported for VV registration [8].

We recommend that image data are obtained under comparable conditions by keeping a similar posture and by taking clinical measures to reduce rectal and bladder filling. We see no reason to suspect that SV registration will be inaccurate when such conditions are met. When images were acquired under much different conditions, such as legs flat and legs raised, rigid-body registration could result in prostate centroid errors as much as 3.4 mm. Another effect may be the tissue deformation from insertion of the RF needle. From our previous experience observing *in vivo* needle insertion in both animal models and clinical trials with real-time MRI, the amount of tissue deformation that occurs with insertion of a sharp bevel tip needle is minimal and transient in tissues with normal interstitial pressure. In certain lesions, such as cysts or necrotic tumor, persistent deformation is possible; however, we can see such deformations in the live-time interventional MRI images and very probably mentally correct the registered, fused images. We previously reported a warping registration method [38], [39] that can correct deformations at the expense of additional complexity, time, and possibly robustness.

The automatic SV registration provides sufficient accuracy for many potential iMRI applications. As compared to a typical SPECT and/or iMRI slice thickness of $\geq$3.0 mm, SV registration is quite accurate. MR spectroscopy also is done at limited resolution. If one were to use functional or high-resolution MR images directly for targeting, the requirements for registration accuracy would be great. However, fused image data will not be used blindly. Rather, these visualizations will be used as a guide. Physicians will always use the live-time iMRI images for needle guidance. With proper visualization tools, they should be able to mentally account for any small registration errors. In addition, very often there is image evidence of cancer in MR prostate images that can perhaps be identified with the aid of functional images. Such MR-visible lesions can then become the markers for tumor targeting.

C. Practicality and Application

The registration experiments presented here provided fairly comprehensive tests for the potential application in iMRI-guided RF thermal ablation of the prostate. Simulation provided an efficient way to extensively evaluate registration performance. The algorithm was extremely robust to noise levels, far beyond those encountered in clinical iMRI applications. Similarly, the inhomogeneity seen with a belt coil was not problematic for transverse images, probably due to coil inhomogeneity simply scaling the grayscale values, an operation that should not affect MI or CC similarity measures. Needle artifacts had little effect, probably because they occupy relatively few voxels. The actual iMRI images acquired under more realistic conditions further tested practicality. Images from the iMRI system contained more noise and had less contrast than those from the 1.5-T scanner. Registration quality was comparable to that of simulation experiments. Registration time can probably be improved considerably using optimized C code rather than IDL. If registration is done in the background in a seamless way, the time for registration is probably quite acceptable. Although we normally used T2-weighted image pairs, the registration worked well for pairs of T1-weighted and T2-weighted images.

We conclude that the automatic SV registration algorithm is quite robust for transverse image slices covering the prostate and that the registration provides sufficient accuracy to aid image-guided therapy. From previous reports of MR-PET or MR-SPECT registration accuracy [6], [7], it appears feasible to combine functional images to aid iMRI-guided procedures. We are beginning to explore this application in animal experiments.

REFERENCES

[1] J. S. Lewin, C. F. Connell, J. L. Duerk, Y. C. Chung, M. E. Clampitt, J. Spisak, G. S. Gazelle, and J. R. Haaga, "Interactive MRI-guided radiofrequency interstitial thermal ablation of abdominal tumors: clinical trial for evaluation of safety and feasibility," *J. Magn. Reson. Imag.*, vol. 8, pp. 40–47, 1998.

[2] D. L. Wilson, A. Carrillo, L. Zheng, A. Genc, J. L. Duerk, and J. S. Lewin, "Evaluation of 3D image registration as applied to MR-guided thermal treatment of liver cancer," *J. Magn. Reson. Imag.*, vol. 8, pp. 77–84, 1998.

[3] A. Carrillo, J. L. Duerk, J. S. Lewin, and D. L. Wilson, "Semiautomatic 3-D image registration as applied to interventional MRI liver cancer treatment," *IEEE Trans. Med. Imag.*, vol. 19, pp. 175–185, Mar. 2000.

[4] D. B. Sodee, N. Malguria, P. Faulhaber, M. I. Resnick, J. Albert, and G. Bakale, "Multicenter ProstaScint imaging findings in 2154 patients with prostate cancer," *Urology*, vol. 56, pp. 988–993, 2000.

[5] J. Scheidler, H. Hricak, D. B. Vigneron, K. K. Yu, D. L. Sokolov, L. R. Huang, C. J. Zaloudek, S. J. Nelson, P. R. Carroll, and J. Kurhanewicz, "Prostate cancer: localization with three-dimensional proton MR spectroscopic imaging—clinicopathologic study," *Radiology*, vol. 213, pp. 473–480, 1999.

[6] D. B. Sodee, G. T. MacLennan, M. I. Resnick, P. F. Faulhaber, Z. Lee, A. D. Nelson, J. P. Molter, and G. Bakale, "Comparison of CT- or MRI-fused PET-FDG and SPECT-ProstaScint® imaging of prostate cancer with the gold standard of histology," *J. Nucl. Med.*, vol. 42, p. 1222, 2001.

[7] Z. Lee, D. B. Sodee, J. L. Duerk, A. D. Nelson, and M. S. Berridge, "Automatic registration of SPECT-MRI in the pelvis," *J. Nucl. Med.*, vol. 41, p. 232, 2000.

[8] B. W. Fei, A. Wheaton, Z. Lee, J. L. Duerk, and D. L. Wilson, "Automatic MR volume registration and its evaluation for the pelvis and prostate," *Phys. Med. Biol.*, vol. 47, pp. 823–838, 2002.

[9] H. Gray, *Anatomy—Descriptive and Surgical* (The classic collector's edition). New York: Gramercy Books, 1977, pp. 823–1010.

[10] B. Kim, J. L. Boes, P. H. Bland, T. L. Chenevert, and C. R. Meyer, "Motion correction in fMRI via registration of individual slices into an anatomical volume," *Magn. Reson. Med.*, vol. 41, pp. 964–972, 1999.

[11] T. S. Kim, M. Singh, W. Sungkarat, C. Zarow, and H. Chui, "Automatic registration of postmortem brain slices to MRI reference volume," *IEEE Trans. Nucl. Sci.*, vol. 47, pp. 1607–1613, Aug. 2000.

[12] J. Zhengping and P. H. Mowforth, "Mapping between MR brain images and voxel model," *Med. Inform.*, vol. 16, pp. 183–193, 1991.
[13] F. Maes, A. Collignon, D. Vandermeulen, G. Marchal, and P. Suetens, "Multimodality image registration by maximization of mutual information," *IEEE Trans. Med. Imag.*, vol. 16, pp. 187–198, 1997.
[14] Y. M. Zhu, "Volume image registration by cross-entropy optimization," *IEEE Trans. Med. Imag.*, vol. 21, pp. 174–180, Feb. 2002.
[15] R. Shekhar and V. Zagrodsky, "Mutual information-based rigid and nonrigid registration of ultrasound volumes," *IEEE Trans. Med. Imag.*, vol. 21, pp. 9–22, Jan. 2002.
[16] J. P. W. Pluim, J. B. A. Maintz, and M. A. Viergever, "Interpolation artefacts in mutual information-based image registration," *Comput. Vis. Image Understand.*, vol. 77, pp. 211–232, 2000.
[17] D. L. G. Hill, L. A. Langsaeter, P. N. Poynter-Smith, P. E. Summers, S. F. Keevil, R. Walsh, D. J. Hawkes, and M. J. Gleeson, "Feasibility study of magnetic resonance imaging-guided intranasal flexible microendoscopy," *Comput. Aided Surg.*, vol. 2, pp. 264–275, 1997.
[18] A. Collignon, F. Maes, D. Delaere, D. Vandermeulen, P. Suetens, and G. Marchal, "Automated multimodality image registration using information theory," in *Proc. 14th Int. Conf. Information Processing in Medical Imaging (IPMI'95)*, 1995, pp. 287–298.
[19] W. H. Press, B. P. Flannery, S. A. Teukolsky, and W. T. Vellerling, *Numerical Recipes in C: The Art of Scientific Computing*, 2nd ed. London, U.K.: Cambridge Univ. Press, 1993.
[20] J. Nelder and R. A. Mead, "A simplex method for function minimization," *Comput. J.*, vol. 7, pp. 308–313, 1965.
[21] M. J. D. Powell, "An iterative method for finding stationary values of a function of several variables," *Comput. J.*, vol. 5, pp. 147–151, 1962.
[22] A. Macovski, "Noise in MRI," *Magn. Reson. Med.*, vol. 36, pp. 494–497, 1996.
[23] R. C. Gregg and R. D. Nowak, "Noise removal methods for high resolution MRI," in *Proc. IEEE Nuclear Science Symp.*, vol. 2, 1997, pp. 1117–1121.
[24] L. Kaufman, D. M. Kramer, L. E. Crooks, and D. A. Ortendahl, "Measuring signal-to-noise ratios in MR imaging," *Radiology*, vol. 173, pp. 265–267, 1989.
[25] R. M. Henkelman, "Measurement of signal intensities in the presence of noise in MR images," *Med. Phys.*, vol. 12, pp. 232–233, 1985.
[26] D. I. Hoult and R. E. Richards, "The signal-to-noise ratio of the nuclear magnetic resonance experiment," *J. Magn. Reson.*, vol. 24, pp. 71–85, 1976.
[27] E. M. Haacke, R. W. Brown, M. R. Thompson, and R. Venkatesan, *Magnetic Resonance Imaging: Physical Principles and Sequence Design*. New York: Wiley, 1999, p. 834.
[28] L. K. Forbes, S. Crozier, and D. M. Doddrell, "Rapid computation of static fields produced by thick circular solenoids," *IEEE Trans. Magn.*, vol. 33, pp. 4405–4410, Sept. 1997.
[29] J. S. Lewin, J. L. Duerk, V. R. Jain, C. A. Petersilge, C. P. Chao, and J. R. Haaga, "Needle localization in MR-guided biopsy and aspiration: effects of field strength, sequence design, and magnetic field orientation," *Amer. J. Roentgenol.*, vol. 166, pp. 1337–1345, 1996.
[30] J. P. W. Pluim, J. B. A. Maintz, and M. A. Viergever, "Image registration by maximization of combined mutual information and gradient information," *IEEE Trans. Med. Imag.*, vol. 19, pp. 809–814, Aug. 2000.
[31] C. Studholme, D. L. G. Hill, and D. J. Hawkes, "Automated three-dimensional registration of magnetic resonance and positron emission tomography brain images by multiresolution optimization of voxel similarity measures," *Med. Phys.*, vol. 24, pp. 25–35, 1997.
[32] D. Rueckert, M. J. Clarke, D. L. G. Hill, and D. J. Hawkes, "Non-rigid registration using higher-order mutual information," in *Proceedings of SPIE*, K. M. Hanson, Ed. Bellingham, WA: SPIE, 2000, vol. 3979, Medical Imaging 2000: Image Processing, pp. 438–447.
[33] F. Maes, "Segmentation and registration of multimodal images: from theory, implementation and validation to a useful tool in clinical practice," Ph.D. dissertation, Katholieke Univ. Leuven, Belgium, 1996.
[34] C. Studholme, D. L. G. Hill, and D. J. Hawkes, "An overlap entropy measure of 3D medical image alignment.," *Pattern Recognit.*, vol. 32, pp. 71–86, 1999.
[35] P. A. Viola, "Alignment by maximization of mutual information," Ph.D. dissertation, Massachusetts Institute of Technology, Cambridge, MA, 1995.
[36] J. M. Fitzpatrick, J. B. West, and C. R. Maurer, "Predicting error in rigid-body point-based registration," *IEEE Trans. Med. Imag.*, vol. 17, pp. 694–702, Oct. 1998.
[37] M. V. Herk, A. Bruce, A. P. G. Kroes, T. Shouman, A. Touw, and J. V. Lebesque, "Quantification of organ motion during conformal radiotherapy of the prostate by three dimensional image registration," *Int. J. Radiat. Oncol. Biol. Phys.*, vol. 33, pp. 1311–1320, 1995.
[38] B.W. Fei, C. Kemper, and D. L. Wilson, "Three-dimensional warping registration of the pelvis and prostate," in *Proceedings of the SPIE* , M. Sonka and J. M. Fitzpatrick, Eds. Bellingham, WA: SPIE, 2002, vol. 4684, Medical Imaging 2002: Image Processing, pp. 528–537.
[39] ——, "A comparative study of warping and rigid body registration for the prostate and pelvic MR volumes," *Comput. Med. Imag. Graph.*, vol. 27, pp. 267–281, 2003.
[40] J. P. W. Pluim, J. B. A. Maintz, and M. A. Viergever, "Mutual information matching in multiresolution contexts," *Image Vis. Comput.*, vol. 19, pp. 45–52, 2001.